Journal of Vacuum Science and Technology A

RESEARCH ARTICLE | MARCH 09 2026

Local slip resistances and critical resolved shear stresses for edge dislocation glide on high-order planes in two refractory multiprincipal element alloys FREE

Special Collection: High Entropy Alloys

Anshu Raj ; Wu-Rong Jian ; Shuozhi Xu

J. Vac. Sci. Technol. A 44, 033201 (2026)
https://doi.org/10.1116/6.0005215
CHORUS

JVST A
Journal of Vacuum Science & Technology A

ARTICLE

pubs.aip.org/avs/jva

Local slip resistances and critical resolved shear stresses for edge dislocation glide on high-order planes in two refractory multiprincipal element alloys

Cite as: J. Vac. Sci. Technol. A 44, 033201 (2026); doi: 10.1116/6.0005215
Submitted: 5 December 2025 · Accepted: 12 February 2026 ·
Published Online: 9 March 2026

Anshu Raj,[1] Wu-Rong Jian,[2,3] and Shuozhi Xu[1,a)]

AFFILIATIONS

[1]School of Aerospace and Mechanical Engineering, University of Oklahoma, Norman, Oklahoma 73019-1052
[2]State Key Laboratory of Subtropical Building Science, South China University of Technology, Guangzhou, Guangdong 510640, People's Republic of China
[3]Department of Engineering Mechanics, South China University of Technology, Guangzhou, Guangdong 510640, People's Republic of China

Note: This paper is part of the Special Topic on High Entropy Alloys.
[a)]**Electronic mail:** shuozhixu@ou.edu

ABSTRACT

Refractory multiprincipal element alloys (RMPEAs) are emerging as promising candidates for extreme-temperature applications; yet, their dislocation-mediated plasticity remains insufficiently understood. Using atomistic simulations, we systematically quantify the local slip resistance (LSR), initial critical resolved shear stress (ICRSS), and CRSS for the glide of an edge dislocation in two RMPEAs (MoNbTi and NbTiZr) and one refractory pure metal (Nb) across {123} and {134} slip planes for both hard- and easy-glide directions. MoNbTi exhibits the highest LSR on the {123} plane for the hard-glide direction (795.84 MPa), more than double that of NbTiZr (344.02 MPa). Both ICRSS and CRSS values show strong line-length dependence. For example, CRSS reaches 897.2 MPa in MoNbTi and 384.2 MPa in NbTiZr at 1 nm—on par with LSR, before converging to plateau stresses of about 370 MPa and about 239 MPa, respectively, beyond 30 nm. The close correspondence between LSR and short-segment ICRSS and CRSS suggests that LSR can be used to indicate the intrinsic slip resistance to a certain degree. Directional anisotropy is more pronounced on the {123} plane than on the {134} plane and is more pronounced in MoNbTi than in NbTiZr. We also find that sometimes in the same material and on the same slip plane, the easy-glide critical stress may surpass its hard-glide counterpart, suggesting a deviation from the theoretical prediction in complex alloys. Taken together, our results advance the understanding of the relationship between chemical complexity and plasticity, pointing toward alloy design strategies for next-generation high-temperature structural materials.

I. INTRODUCTION

For decades, alloy design has centered on tuning a dominant matrix element with minor solute additions—a strategy that confined discovery to the outer edges of multicomponent phase diagrams.[1–3] This paradigm shifted in 2004 when Yeh *et al.*[4] and Cantor *et al.*[5] demonstrated that carefully designed multicomponent alloys could form stable solid-solution phases rather than brittle intermetallics, giving rise to the field of multiprincipal element alloys (MPEAs).[6,7] Defined as alloys containing three or more principal elements on simple face-centered cubic or body-centered cubic (BCC) lattices, MPEAs exhibit exceptional combinations of strength, ductility, and damage tolerance.[8,9] Since 2010, refractory MPEAs (RMPEAs),[10] which predominantly consist of high-melting-point elements, such as Mo, Nb, Ta, W, V, Hf, and Ti, have garnered significant attention due to their exceptional high-temperature mechanical properties. Alloys, such as MoNbTaW and MoNbTaVW, for instance, exhibit

specific yield strengths that are approximately two to four times greater than those of conventional high-temperature alloys, such as Inconel 718 and Haynes 230 at 1000 °C.[11] While many RMPEAs crystallize in the BCC structure, a limited number of them form a single BCC phase and have been reported to retain high strength beyond 1200 °C, surpassing conventional Ni-based superalloys.[12] This contrasts with conventional BCC alloys, which have a strong temperature dependence of mechanical properties. The combination of superior thermal stability, oxidation resistance, and high-temperature performance highlights RMPEAs as prime candidates for next-generation structural applications in aerospace, energy, and nuclear technologies.[10,12,13]

In BCC pure metals, dilute BCC alloys, and RMPEAs, the plastic deformation is governed by dislocation dynamics. To quantify the dislocation motion, two key descriptors are usually adopted: local slip resistance (LSR) and critical resolved shear stresses (CRSS). The LSR measures the minimum stress needed for a very short dislocation segment (typically less than 1 nm) to move by at least 1 nm.[14] By contrast, CRSS reflects the stress required to drive a much longer dislocation line through the lattice. In pure metals, the motion of a short dislocation is uniform inside the material; thus, LSR is reduced to the Peierls stress. For a long dislocation at low homologous temperatures, the line is largely straight during motion, although local kinks or jogs may occur, as plasticity-dominated screw dislocations primarily move through kink-pair mechanisms.[15,16] In RMPEAs, the local barriers to dislocation motion are spatially variable, leading to a corresponding spatial variation in the LSR. As a result, the motion of a long dislocation becomes wavy, reflecting the rugged underlying energy landscape.[17–19]

The strikingly different dislocation behaviors in BCC pure metals and RMPEAs are reflected by their differences in LSR and CRSS. Four key findings are as follows. First, the screw-to-edge ratios in LSR and CRSS are significantly reduced in RMPEAs compared with pure BCC metals.[20] Computationally, calculations of LSR and CRSS to date have heavily relied on atomistic simulations, because they explicitly capture the influence of local chemical fluctuations, lattice distortion (LD), and kink interactions that are inaccessible to continuum models. Based on simulations, the reduction in the screw-to-edge ratio has been reported in dozens of RMPEAs by Xu *et al.*,[14] Romero *et al.*,[21] Nitol *et al.*,[22] Wang *et al.*,[23] and Jian *et al.*[24] Consequently, edge dislocations, which play only a secondary role in the plasticity of BCC pure metals, contribute comparably to screw dislocations in some RMPEAs.[25,26] The second finding is that while slips chiefly occur on low-order {110} and {112} planes in BCC pure metals, they frequently appear on high-order planes, such as {123} and {134}.[27] High-order slip planes have been suggested to play a role in intermediate-temperature deformation mechanisms in RMPEAs, with dipole dragging proposed as one possible contributor to the strength plateau observed near $0.6T_m$.[28] The third finding is that the CRSS strongly depends on the dislocation line length in RMPEAs, compared with BCC pure metals in which the weaker length dependence is a result of the plasticity-dominated screw dislocation moving through kink-pair mechanisms.[15,16] For example, Xu *et al.*[29] demonstrated that in MoNbTi and NbTiZr, CRSS becomes length-independent beyond 30 nm, in agreement with analytical models. The last finding, also concerning CRSS, is that a long dislocation starts moving in an MPEA via the bow-out of a small dislocation segment, corresponding to the initial CRSS (ICRSS).[30] As the strain increases, other segments begin to move, though they are often pinned again after a short distance by local fluctuations in stacking fault energy or LD,[31–33] giving rise to a stepwise progression of glide. At sufficiently high stress, the dislocation line finally sweeps through the simulation cell, which defines the overall CRSS.

Despite these advances, three critical knowledge gaps remain. First, past studies have treated LSR and CRSS separately; a direct comparison between them for short dislocations has not been made. Second, while some LSR values were calculated on high-order planes,[14,24] most CRSS studies have focused on low-order {110} and {112} planes.[29] A key question is whether the line-length dependencies of CRSS are similar on different slip planes. Third, the role of glide-direction anisotropy has been overlooked. Specifically, on all four potential slip planes except {110}, there exists an "easy-glide" direction, associated with a relatively low CRSS, and its opposite, a "hard-glide" direction, which is accompanied by a higher CRSS. A notable example is the twinning (easy) and antitwinning (hard) glides on {112} planes.[20,27]

In this work, we address all three knowledge gaps by systematically comparing the LSR, ICRSS, and CRSS across multiple slip planes and glide directions in two representative RMPEAs—MoNbTi and NbTiZr—as well as in pure Nb. By examining short dislocation segments across all systems, we are able to make a direct comparison between LSR and ICRSS: the two quantities nearly coincide, confirming that the LSR reflects the intrinsic lattice resistance. Second, extending the analysis to the higher-order {123} plane shows a similar line-length dependence of the CRSS compared with lower-order planes. Finally, contrasting easy- and hard-glide directions on each plane highlights slip-direction anisotropy in both RMPEAs, with MoNbTi consistently exhibiting higher resistances—often by several hundred MPa than NbTiZr. Together, these results demonstrate that lattice resistance, dislocation length, slip plane, and glide-direction anisotropy collectively shape dislocation glide in RMPEAs, providing a basis for designing compositions with targeted strength and plasticity.

II. METHODS

A. Materials

In this study, we mainly examine two RMPEAs, MoNbTi and NbTiZr. These two alloys were chosen as a direct continuation of our earlier work on LSR[14,24] and CRSS[29] in RMPEAs. In addition to the two RMPEAs, we examine three reference systems: two artificial *A*-atom systems (denoted as $MoNbTi_A$ and $NbTiZr_A$), in which all atoms share identical synthetic interaction parameters, and one physical elemental metal, Nb. The *A*-atom systems provide idealized reference models with chemically homogeneous environments on a BCC lattice, enabling the isolation of lattice structure effects from chemical complexity; they are not intended to represent any elemental metals.

B. Software

All atomistic simulations were carried out using LAMMPS,[34] which is widely employed for accurate and scalable modeling of

metallic systems. The crystalline structures of all materials were prepared using Atomsk,[35] a platform for generating and modifying atomic configurations. Postprocessing and visualization were performed with OVITO.[36]

C. Interatomic potentials

Interatomic interactions in all materials were described using the embedded-atom method (EAM) potential,[37] a well-established formalism for metallic alloys that accounts for many-body effects by embedding atoms into a host electron density field. Unlike simple pair potentials, the EAM framework incorporates collective atomic interactions, enabling a more realistic description of alloy energetics and defect behavior. The total energy is expressed as

$$E = \frac{1}{2}\sum_{i=1}^{N}\sum_{j=1j\neq i}^{N_{\text{nei}}} V(R^{ij}) + \sum_{i=1}^{N} F(\rho^i), \tag{1}$$

where N is the total number of atoms, N_{nei} is the number of neighbors surrounding atom i, $V(R^{ij})$ is the pair potential between atoms i and j, and $F(\rho^i)$ is the embedding function of the host electron density ρ^i. The interatomic distance is

$$R^{ij} = R^j - R^i, \tag{2}$$

with the host electron density defined as

$$\rho^i = \sum_{j=1j\neq i}^{N_{\text{nei}}} \rho^j(R^{ij}), \tag{3}$$

where $\rho^j(R^{ij})$ represents the electron density contribution from atom j. Importantly, the forms of V and $\rho^j(R^{ij})$ depend only on the type of atom i and the interatomic distance R^{ij}, independent of the chemical identity of atom j. This many-body description enables the EAM potential to capture alloy-specific energetics with much higher fidelity than pairwise models, making it particularly suitable for complex concentrated alloys. EAM parameters used here for both alloys and pure metals are taken from previous work: MoNbTi[38] and NbTiZr.[39]

The A-atom EAM formulation for the potential energy is[40,41]

$$E = \frac{1}{2}\sum_{i}^{N}\sum_{j\neq i}^{N_{\text{nei}}} V_{ij}^{A}(R^{ij}) + \sum_{i}^{N} F^{A}(\langle\bar{\rho}_i\rangle), \tag{4}$$

where

$$F^{A}(\langle\bar{\rho}_i\rangle) = \sum_{X}^{N_{\text{T}}} c^X F^X(\langle\bar{\rho}_i\rangle), \tag{5}$$

$$V_{ij}^{A}(R^{ij}) = \sum_{X,Y}^{N_{\text{T}}} c^X c^Y V_{ij}^{XY}(R^{ij}), \tag{6}$$

$$\langle\bar{\rho}_i\rangle = \sum_{j\neq i}^{N_{\text{nei}}}\sum_{X}^{N_{\text{T}}} c^X \rho_{ij}^{X}(R^{ij}), \tag{7}$$

where N_{T} is the number of elemental types, and c^X and c^Y are atomic concentrations of elements X and Y, respectively.

D. LSR calculations

A schematic of the simulation cell is shown in Fig. 1(a). The cell size is $L_x = 40$ nm, $L_y = 50$ nm, and $L_z = 1$ nm, with a total atom count ranging from 293 160 to 408 330 depending on whether the {123} or {134} slip plane is considered. We employ the stacked-block method proposed by Osetsky and Bacon.[42] In this procedure, two crystal blocks are created: the upper block is assigned an extra half-plane (an additional column of atoms) and compressed by half a Burgers vector, while the lower block is stretched by the same amount. Once the sizes of the blocks match along the x direction, they are joined seamlessly along the y direction and relaxed. As a result, the dislocation line is positioned at the midslip plane of each cell, consistent with prior modeling work.[43,44] Periodic boundary conditions (PBCs) are applied along the dislocation glide direction (x) and the dislocation line direction (z), while traction-free boundaries are imposed along y. This cell is called "periodic array of dislocations," which has been demonstrated to be well suited for evaluating Peierls stresses and LSR in BCC materials.[23,45]

To drive dislocation motion, an incremental shear strain tensor with a single nonzero component was applied to the simulation cell, resulting in forward ($+x$) and backward ($-x$) glide of the edge dislocation. The crystallographic orientations, summarized in Table I, are set such that the forward and backward glide, respectively, are the hard- and easy-glide. A strain increment of 10^{-5} per step was used, followed by energy minimization using the conjugate gradient algorithm after each increment. During relaxation, atoms in the y-boundary layers were constrained to relax only along the x and z directions, while all remaining atoms were free to move in all three directions. At the end of each energy minimization, the corresponding virial stress is recorded. The LSR was determined as the minimum virial stress at which the dislocation is advanced by at least 1 nm from its initial position. In other words, LSR is calculated at 0 K using molecular statics (MS), rather than molecular dynamics (MD), ensuring that the measured resistance corresponds to the intrinsic lattice friction at 0 K.

To capture the randomness in atomistic distribution in MPEAs, ten independent atomic structures were generated for each dislocation type and slip system. In this paper, both the mean value and the standard deviation for LSR are reported.

E. ICRSS and CRSS calculations

For the ICRSS and CRSS calculations, we used simulation cells with the same boundary conditions and crystallographic orientations as in the LSR calculations. The dislocation line was aligned with the z direction, and its initial length is denoted as L_0; in other words, $L_z = L_0$. To examine the line-length dependence, L_z was varied from 1 to 50 nm, while the edge lengths of the cell along the other two directions are fixed: $L_x = 40$ nm and $L_y = 50$ nm. Figure 1(b) illustrates the cell with L_z being 30 nm. Similar to the LSR case, an edge dislocation is inserted on the mid-y plane using the stacked-block method. We remark that the L_x/L_y ratio in all

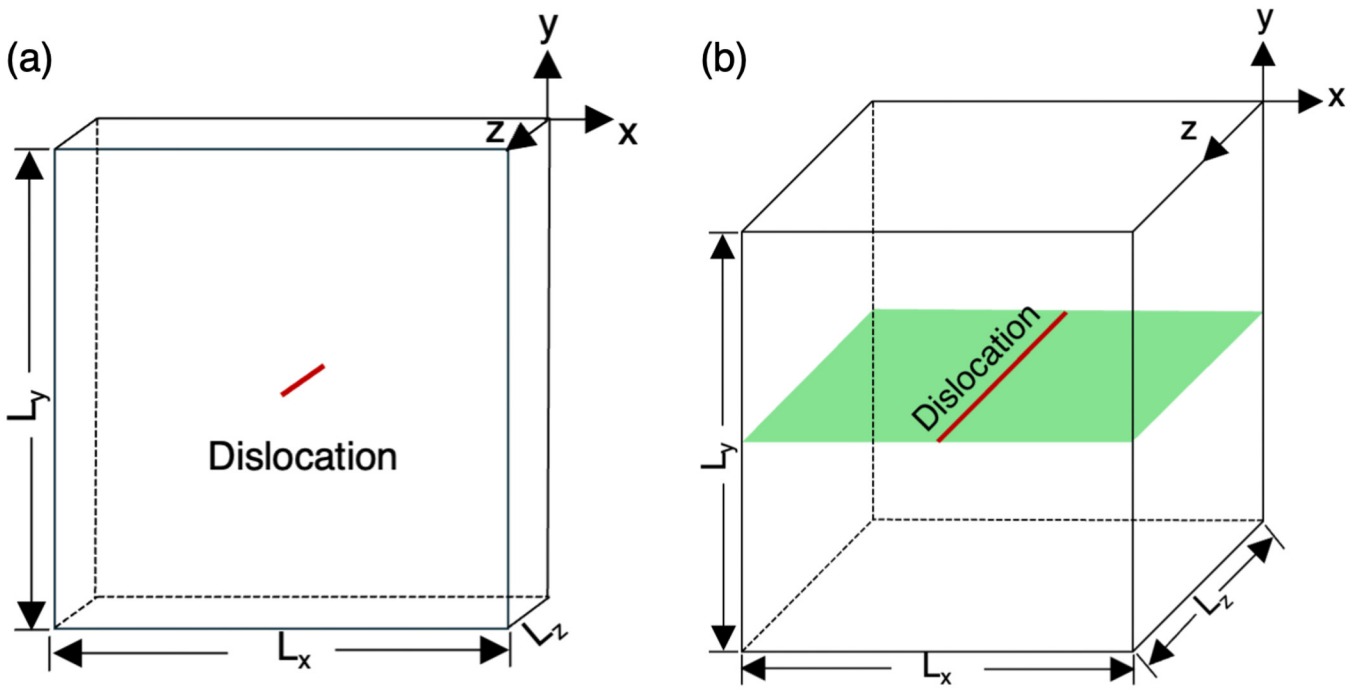

FIG. 1. Schematics of the simulation cells used to calculate (a) the LSR and (b) the CRSS of a single dislocation.

calculations in this paper follows Szajewski and Curtin[46] to minimize the spurious image forces caused by the PBCs.

Each system is first relaxed dynamically for 10 ps using an NVT ensemble at 5 K with a Nosé–Hoover thermostat to remove residual stresses without triggering thermally activated glide.[30] It follows that a shear strain tensor $\Delta\varepsilon$ with a single nonzero off-diagonal component was applied to each simulation cell, with all other components set to zero. A constant strain rate of 10^7 s^{-1} is employed, using the same forward (hard-glide) and backward (easy-glide) shear directions as in the LSR setup. Along the y axis, the simulation domain was partitioned into boundary regions, buffer regions, and a central region containing the dislocation. During deformation, atoms in the boundary regions were continuously displaced to impose shear through flexible boundary conditions, while buffer regions were maintained at 5 K using an NVT ensemble. The remaining regions were evolved under an NVE ensemble.[47] In other words, unlike the use of MS simulations in calculating the LSR, full MD simulations are employed here.

TABLE I. Crystallographic orientations of the simulation cells for both LSR and CRSS calculations on {123} and {134} slip planes.

	x	y	z
{123}	[111]	$[\bar{1}\bar{2}3]$	$[5\bar{4}\bar{1}]$
{134}	[111]	$[31\bar{4}]$	$[\bar{5}7\bar{2}]$

During the shear loading, we monitored the virial shear stress and tracked the dislocation position. The initial CRSS (ICRSS) was defined as the stress peak associated with the first dislocation segment bow-out event. The CRSS was taken as the stress level that is sufficiently high to allow for continuous dislocation glide across the cell. We remark that at finite temperatures, the reported ICRSS and CRSS values should be interpreted as effective critical stresses defined by the applied strain rate and observation time, rather than as absolute thresholds for dislocation motion at those temperatures. In addition, because the strain rate used here is several orders of magnitude higher than those in most experiments, our ICRSS and CRSS values do not directly reproduce experimentally measured strengths.

To capture the variability in the random atomic distribution, we determined five ICRSS and five CRSS values for each dislocation line length on each slip plane in each alloy. In the remainder of this paper, both mean values and standard deviation for ICRSS and CRSS are reported.

III. RESULTS AND DISCUSSION

A. LSR calculation results

The LSR values for the {123} and {134} slip planes along both "hard-glide" and "easy-glide" directions are presented in Table II. Results exhibit trends influenced by composition, slip plane type, and glide direction. On the {123} plane, the hard-glide direction in MoNbTi yielded the highest mean LSR, measured at

TABLE II. LSR for different materials, slip planes, and glide directions.

Material	Nb		MoNbTi		NbTiZr	
Slip plane	{123}	{134}	{123}	{134}	{123}	{134}
Easy-glide	13 (Ref. 14)	13 (Ref. 14)	573.74 ± 233.31	561.76 ± 307.80	424.39 ± 232.97	388.54 ± 198.91
Hard-glide	12 (Ref. 14)	12 (Ref. 14)	795.84 ± 282.66 (Ref. 24)	741.89 ± 120.02	344.02 ± 121.35 (Ref. 24)	436.51 ± 218.62

795.84 ± 282.66 MPa, compared with 344.02 ± 121.35 MPa in NbTiZr. For the easy-glide direction, MoNbTi showed a lower mean LSR of 573.74 ± 233.31 MPa, while NbTiZr exhibited a higher mean value of 424.39 ± 232.97 MPa. In terms of the symmetry, however, the relatively large standard deviations lead to substantial overlap between hard- and easy-glide LSR ranges, particularly in NbTiZr, indicating that these directional differences should be interpreted as qualitative trends rather than statistically resolved asymmetries.

A similar pattern was observed on the {134} plane. MoNbTi again displayed higher mean LSR values than NbTiZr for both shearing directions—741.89 ± 120.02 vs 436.51 ± 218.62 MPa in the hard-glide direction and 561.76 ± 307.80 vs 388.54 ± 198.91 MPa in the easy-glide direction. While the mean differences between glide directions on this plane are smaller than those on the {123} plane, the overlapping uncertainty ranges suggest that any directional anisotropy is modest and slip-plane dependent.

These qualitative trends can be discussed in the context of differences in elemental contributions and local lattice resistance in the two alloys. In particular, Mo is known to exhibit a relatively high Peierls stress compared with other BCC refractory elements,[14] which may contribute to the higher mean LSR values observed in MoNbTi.

B. CRSS calculation results

1. MoNbTi: ICRSS

ICRSS for dislocation glide on the {123} plane along the hard-glide direction in MoNbTi is calculated as a function of dislocation line length. As presented in Fig. 2(a), the ICRSS exhibits a nonmonotonic dependence on line length: it decreases from 747.4 ± 172.4 MPa at 1 nm to a minimum of 331.2 ± 55.31 MPa at 20 nm, followed by an increase to 418.9 ± 36.16 MPa at 50 nm. This behavior reflects a complex interplay between line tension

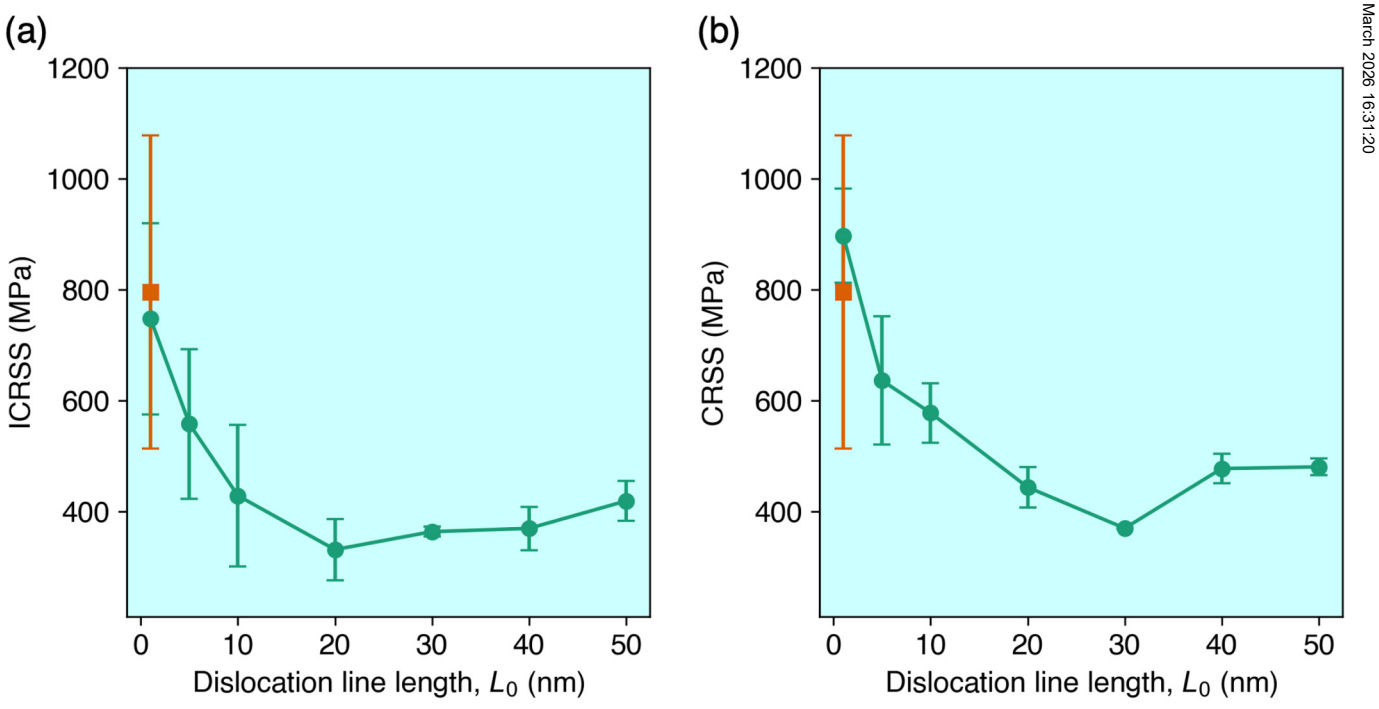

FIG. 2. (a) ICRSS and (b) CRSS for dislocation glide on the {123} plane along the hard-glide direction in MoNbTi. In each subfigure, the square indicates the LSR on the {123} plane along the hard-glide direction in MoNbTi.

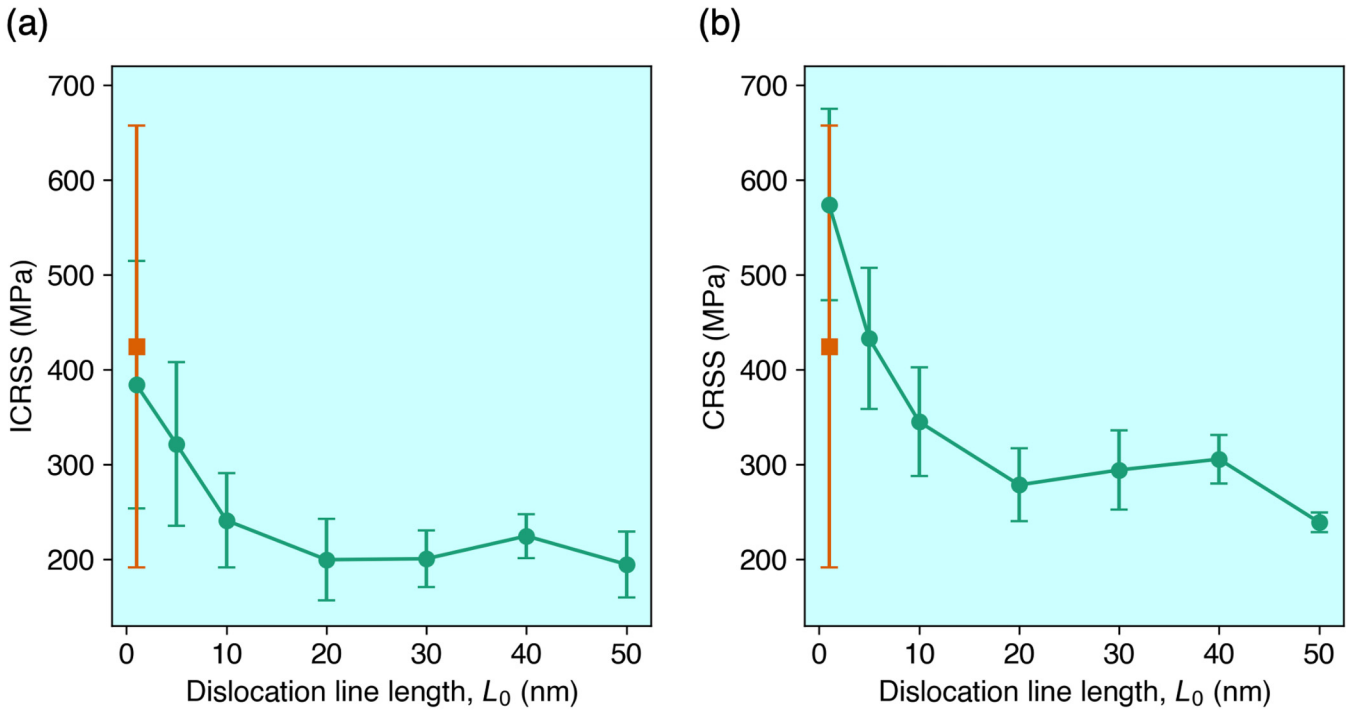

FIG. 3. (a) ICRSS and (b) CRSS for dislocation glide on the {123} plane along the easy-glide direction in NbTiZr. In each subfigure, the square indicates the LSR on the {123} plane along the easy-glide direction in NbTiZr.

effects, which dominate at shorter dislocation lengths, and long-range stress field relaxation or image forces that become more prominent as the line extends. Notably, for a 1 nm dislocation line, the mean ICRSS (747.4 MPa) is slightly lower than the mean LSR (795.84 MPa). Interestingly, with a line length of 50 nm, the easy-glide ICRSS is 456.2 ± 27.22 MPa, higher than the hard-glide counterpart (418.9 MPa), suggesting that the directional critical stress ranking can be altered while the dislocation line length is long.

On the {134} plane and with a line length of 50 nm, the corresponding ICRSS values are 370.8 ± 32.15 MPa for the easy-glide direction and 323 ± 46.66 MPa for the hard-glide direction, revealing a similar directionality as the {123} plane. In agreement with the LSR, ICRSS for the {123} plane is higher than that for the {134} plane, regardless of the glide direction.

2. MoNbTi: CRSS

Increasing the strains in the same simulations for ICRSS calculation will lead to CRSS, which is the maximum stress required for the dislocation to glide through the entire simulation cell. Figure 2(b) shows the CRSS on the {123} plane along the hard-glide direction in MoNbTi as a function of dislocation line length. At the shortest segment length of 1 nm, the CRSS is 897.2 ± 84.77 MPa, followed by a substantial drop to 636 ± 115.47 MPa at 5 nm. The lowest CRSS is observed near 30 nm (369.67 ± 1.15 MPa), beyond which a moderate increase is noted, with CRSS being 480.4 ± 14.94 MPa at the longest dislocation line of 50 nm. Similar to ICRSS, the CRSS for the easy-glide direction (504 ± 19.43 MPa) is higher than that for the hard-glide direction, further indicating the line-length-dependent directionality in critical stress.

On the {134} slip plane, the CRSS values at 50 nm are nearly symmetric—424.8 ± 23.19 MPa for the easy-glide direction and 420.6 ± 38.71 MPa for the hard-glide direction. Both of them are lower than their counterparts on the {123} slip plane, in agreement with both LSR and ICRSS.

3. NbTiZr: ICRSS

Figure 3(a) presents data similar to Fig. 2(a), except that the material is NbTiZr and the direction is easy-glide. On the {123} plane, a progressive decline in ICRSS is evident with increasing dislocation length: from 384.2 ± 130.4 MPa at 1 nm to a minimum of 194.8 ± 34.58 MPa at 50 nm. Intermediate data points show a steep drop at short lengths (5–10 nm), followed by a relatively stable regime between 20 and 40 nm, where the stress varies narrowly between 199.8 and 224.8 MPa. Similar to MoNbTi, the mean ICRSS for a 1 nm dislocation line is slightly lower than the mean LSR (424.39 MPa). In addition, at a line length of 50 nm, the hard-glide ICRSS is 208.8 ± 21.57 MPa, which is higher than its easy-glide counterpart, a trend that contrasts the LSR.

On the {134} plane and with a line length of 50 nm, the ICRSS values are 189.2 ± 25.41 MPa for the easy-glide direction and 199.2 ± 29.84 MPa for the hard-glide direction. Both of them are very close to those for the {123} plane, suggesting a diminished slip-plane and slip-direction anisotropy in ICRSS in NbTiZr compared with MoNbTi.

4. NbTiZr: CRSS

Figure 3(b) presents the CRSS on the {123} slip plane for the easy-glide direction as a function of the dislocation line length. Similar to ICRSS, the CRSS exhibits a pronounced length-dependent trend. Starting at 573.8 ± 100.88 MPa for a 1 nm dislocation segment, the stress required for glide decreases sharply to 433 ± 74.19 MPa at 5 nm and further to 345.1 ± 57.38 MPa at 10 nm. A more gradual reduction follows, reaching 278.6 ± 38.45 MPa at 20 nm and eventually 239.2 ± 10.64 MPa at 50 nm. For the hard-glide direction on the same plane, the CRSS at 50 nm, 234.2 ± 17.81 MPa, is slightly lower than its easy-glide counterpart, a trend that contrasts ICRSS but agrees with LSR.

On the {134} plane, the CRSS values at 50 nm remain nearly symmetric—230.8 ± 4.44 MPa and 239.4 ± 15.57 MPa for easy- and hard-glide directions, respectively—reaffirming the reduced anisotropy associated with this slip plane and this material.

5. Pure metals

To provide references to the two RMPEAs, CRSS in three pure metals are also calculated. Figure 4 shows CRSS on the {123} slip plane along the hard-glide or easy-glide direction as a function of dislocation line length.

We first focus on Nb. A subtle nonmonotonic trend is observed: the CRSS increases from 16 MPa at a line length of 1 nm to a peak of 19 MPa at intermediate lengths (20 and 30 nm), followed by a slight decline to 16 MPa at 40 and 50 nm. Interestingly, the 1 nm CRSS is a bit higher than the LSR counterpart (12 MPa) for the same hard-glide direction, contrasting the observation for the two RMPEAs. Along the easy-glide direction on the same slip plane, the CRSS at 50 nm is 13 MPa, slightly lower than its hard-glide counterpart (16 MPa). On the {134} plane, the CRSS at 50 nm is 13 and 14 MPa, respectively, for the easy- and hard-glide directions, reflecting a slightly reduced sensitivity of CRSS to glide direction on this plane.

Extending this analysis to MoNbTi$_A$, a similar line-length-dependent behavior emerges. Along the hard-glide direction on the {123} plane, the CRSS starts at 17 MPa for the shortest line (1 nm), then it drops to 13 MPa at 5 nm, and remains nearly constant until 12 MPa at 50 nm. The easy-glide direction on the same plane shows a CRSS of 13 MPa at 50 nm, almost identical to the hard-glide value, highlighting minimal directional dependence in this pure metal. On the {134} plane, however, the asymmetry becomes more pronounced: the easy-glide CRSS at 50 nm is only 11 MPa, whereas the hard-glide value increases to 19 MPa.

Lastly, NbTiZr$_A$ displays a distinct line-length dependent trend. Along the easy-glide direction on the {123} plane, the CRSS remains constant at 47 MPa across all line lengths from 1 to 50 nm, indicating an absence of any measurable size effect. The hard-glide CRSS at 50 nm exhibits a higher CRSS of 64 MPa than its easy-glide counterpart. A similar phenomenon is observed on the {134} plane, where the easy- and hard-glide CRSS values reach 42 and 62 MPa, respectively.

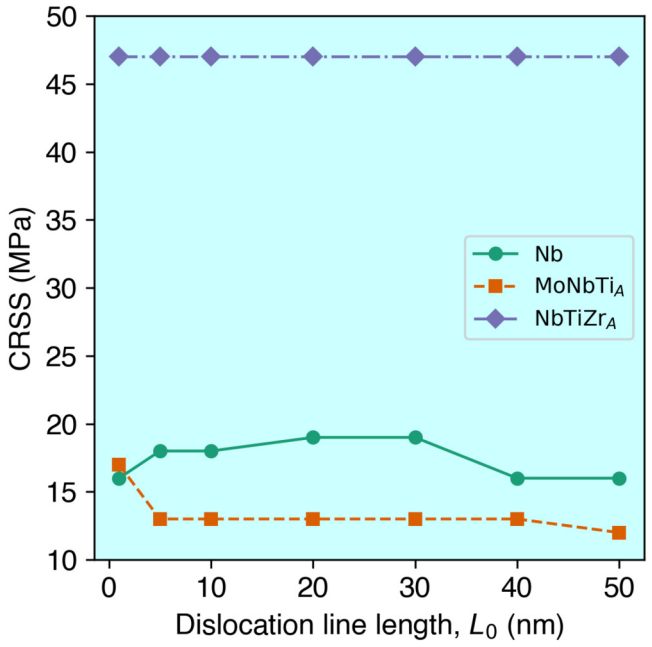

FIG. 4. CRSS for dislocation glide on the {123} plane along the hard-glide direction in Nb and MoNbTi$_A$, and along the easy-glide direction in NbTiZr$_A$.

Interestingly, the CRSS in NbTiZr$_A$ along the easy-glide direction on the {123} plane, 47 MPa, is higher than the CRSS in MoNbTi$_A$, while the alloy potentials predict that MoNbTi has a higher CRSS than NbTiZr. Similar results were found on the {110} and {112} planes,[29] suggesting that conclusions based on *A*-atom potentials should be taken with caution.

C. Comparison between low-order and high-order planes

Figure 5 summarizes the LSR and CRSS across all four slip planes in MoNbTi, NbTiZr, and Nb, based on data both newly generated in this paper and reported in our previous work.[14,24,29] In most cases, on the same plane, the LSR values are notably elevated relative to their CRSS counterparts. Take the easy-glide direction in MoNbTi as an example: 797.49 ± 321.13 MPa (LSR)[24] vs 327.6 ± 13.78 MPa (CRSS)[29] on the symmetric {110} plane; 1085.82 ± 425.87 MPa (LSR)[24] vs 498 ± 19.2 MPa (CRSS)[29] on {112}. In addition, values of the LSR and CRSS, as well as the quantitative disparity between them, are different across different slip planes. In the pure metal Nb and the low-LD alloy MoNbTi, the magnitude of both LSR and CRSS is the highest for the {112} slip plane, while their corresponding values on the other three operative planes remain relatively similar. As recently found by Jian *et al.*[24] in high-LD alloys, such as NbTiZr, the LSR and CRSS on the {110} plane tend to be higher than those on high-order planes.

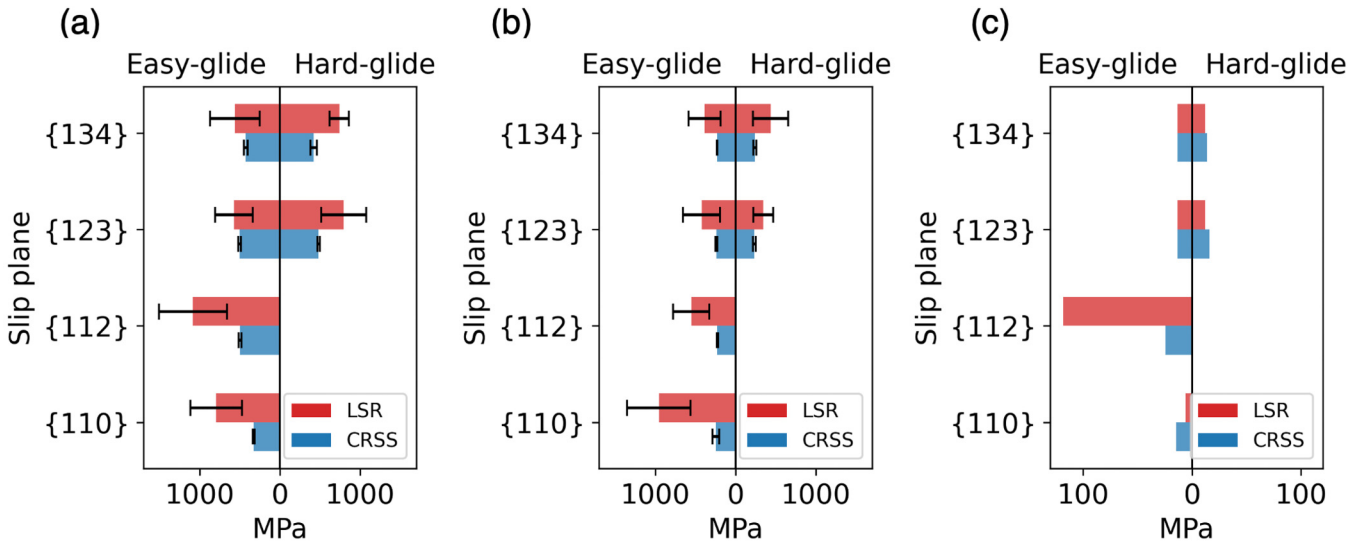

FIG. 5. Comparison of LSR and CRSS for easy- and hard-glide directions across four slip planes in (a) MoNbTi, (b) NbTiZr, and (c) Nb. Note that the two directions are symmetric on {110} planes. CRSS is taken for a dislocation line length of 50 nm.

Furthermore, concerning the difference between LSR and CRSS, a discernible trend is that low-order planes are correlated with a larger difference compared to high-order planes.

IV. CONCLUSIONS

In this study, we used atomistic simulations to examine LSR, ICRSS, and CRSS associated with edge dislocation glide in two RMPEAs, MoNbTi and NbTiZr, as well as in pure Nb. The simulations were set up to systematically probe the roles of dislocation line length, slip plane, and glide direction in determining lattice resistance.

For short dislocation segments, the mean LSR values were found to be close to the corresponding ICRSS values, suggesting that LSR captures the intrinsic lattice resistance experienced by short segments. As the dislocation length increases, the CRSS shows a strong length dependence and gradually approaches a plateau beyond roughly 30 nm, consistent with trends reported previously for lower-order planes in RMPEAs.

The results also indicate that slip-plane and glide-direction effects on LSR, ICRSS, and CRSS are more evident in MoNbTi than in NbTiZr, although the differences should be viewed as qualitative given the overlap in uncertainty ranges. In several cases, the relative magnitudes of hard- and easy-glide critical stresses vary with dislocation length and slip plane. These findings, combined with the substantial increase in lattice resistance in RMPEAs compared with pure Nb, reflect the complex interactions among local chemical fluctuations, slip geometry, and dislocation length in BCC metallic materials.

ACKNOWLEDGMENTS

Some of the computing for this project was performed at the OU Supercomputing Center for Education & Research at the University of Oklahoma (OU). A.R. and S.X. acknowledge the support of the U.S. National Science Foundation (No. DMREF-2522655).

AUTHOR DECLARATIONS

Conflict of Interest

The authors have no conflicts to disclose.

Author Contributions

Anshu Raj: Data curation (equal); Formal analysis (lead); Methodology (equal); Software (lead); Writing – original draft (lead). **Wu-Rong Jian:** Data curation (equal); Methodology (equal). **Shuozhi Xu:** Conceptualization (lead); Funding acquisition (lead); Project administration (lead); Supervision (lead); Writing – review & editing (lead).

DATA AVAILABILITY

The data that support the findings of this study are openly available in GitHub at https://github.com/shuozhixu/JVSTA_2026, Ref. 48.

REFERENCES

[1]I. J. Beyerlein, S. Xu, J. Llorca, J. A. El-Awady, J. R. Mianroodi, and B. Svendsen, MRS Bull. **44**, 257 (2019).
[2]H. Y. Diao, R. Feng, K. A. Dahmen, and P. K. Liaw, Curr. Opin. Solid State Mater. Sci. **21**, 252 (2017).
[3]Y. Ye, Q. Wang, J. Lu, C. Liu, and Y. Yang, Mater. Today **19**, 349 (2016).
[4]J.-W. Yeh, S.-K. Chen, S.-J. Lin, J.-Y. Gan, T.-S. Chin, T.-T. Shun, C.-H. Tsau, and S.-Y. Chang, Adv. Eng. Mater. **6**, 299 (2004).

[5]B. Cantor, I. T. H. Chang, P. Knight, and A. J. B. Vincent, Mater. Sci. Eng. A **375–377**, 213 (2004).
[6]E. J. Pickering and N. G. Jones, Int. Mater. Rev. **61**, 183 (2016).
[7]A. Takeuchi, K. Amiya, T. Wada, K. Yubuta, and W. Zhang, JOM **66**, 1984 (2014).
[8]E. P. George, D. Raabe, and R. O. Ritchie, Nat. Rev. Mater. **4**, 515 (2019).
[9]D. B. Miracle and O. N. Senkov, Acta Mater. **122**, 448 (2017).
[10]O. N. Senkov, D. B. Miracle, K. J. Chaput, and J.-P. Couzinie, J. Mater. Res. **33**, 3092 (2018).
[11]O. N. Senkov, G. B. Wilks, J. M. Scott, and D. B. Miracle, Intermetallics **19**, 698 (2011).
[12]B. G. Butler, J. D. Paramore, J. P. Ligda, C. Ren, Z. Z. Fang, S. C. Middlemas, and K. J. Hemker, Int. J. Refract. Met. Hard Mater. **75**, 248 (2018).
[13]O. Senkov, G. Wilks, D. Miracle, C. Chuang, and P. Liaw, Intermetallics **18**, 1758 (2010).
[14]S. Xu, Y. Su, W.-R. Jian, and I. J. Beyerlein, Acta Mater. **202**, 68 (2021).
[15]S. Queyreau, J. Marian, M. Gilbert, and B. Wirth, Phys. Rev. B **84**, 064106 (2011).
[16]T. Swinburne, S. Dudarev, S. Fitzgerald, M. Gilbert, and A. Sutton, Phys. Rev. B **87**, 064108 (2013).
[17]Y. Cheng, E. Bitzek, D. Weygand, and P. Gumbsch, Modell. Simul. Mater. Sci. Eng. **18**, 025006 (2010).
[18]A. Raj, J. Brechtl, S. Mubassira, P. K. Liaw, and S. Xu, Mater. Lett. **400**, 139038 (2025).
[19]T. Okita, K. Asari, S. Fujita, and M. Itakura, Fusion Sci. Technol. **66**, 289 (2014).
[20]K. Kang, V. V. Bulatov, and W. Cai, Proc. Natl. Acad. Sci. U.S.A. **109**, 15174 (2012).
[21]R. A. Romero, S. Xu, W.-R. Jian, I. J. Beyerlein, and C. Ramana, Int. J. Plast. **149**, 103157 (2022).
[22]M. S. Nitol, M. J. Echeverria, K. Dang, M. I. Baskes, and S. J. Fensin, Comput. Mater. Sci. **237**, 112886 (2024).
[23]T. Wang, J. Li, M. Wang, C. Li, Y. Su, S. Xu, and X.-G. Li, npj Comput. Mater. **10**, 143 (2024).
[24]W.-R. Jian, A. S. Kulathuvayal, H. Zhai, A. Raj, X. Yao, Y. Su, S. Xu, and I. J. Beyerlein, Int. J. Plast. **199**, 104635 (2026).
[25]C. Lee *et al.*, Nat. Commun. **12**, 5474 (2021).
[26]C. Lee *et al.*, Sci. Adv. **6**, eaaz4748 (2020).
[27]F. Wang *et al.*, Science **370**, 95 (2020).
[28]F. Maresca and W. A. Curtin, Acta Mater. **182**, 235 (2020).
[29]S. Xu, W.-R. Jian, Y. Su, and I. J. Beyerlein, Appl. Phys. Lett. **120**, 061901 (2022).
[30]L. T. W. Fey, S. Xu, Y. Su, A. Hunter, and I. J. Beyerlein, Phys. Rev. Mater. **6**, 013605 (2022).
[31]S. Hayakawa, K. Doihara, T. Okita, M. Itakura, M. Aichi, and K. Suzuki, J. Mater. Sci. **54**, 11509 (2019).
[32]K. Asari, O. Hetland, S. Fujita, M. Itakura, and T. Okita, J. Nucl. Mater. **442**, 360 (2013).
[33]K. Doihara, T. Okita, M. Itakura, M. Aichi, and K. Suzuki, Philos. Mag. **98**, 2061 (2018).
[34]A. Thompson *et al.*, Comput. Phys. Commun. **271**, 108171 (2022).
[35]P. Hirel, Comput. Phys. Commun. **197**, 212 (2015).
[36]A. Stukowski, Modell. Simul. Mater. Sci. Eng. **18**, 015012 (2010).
[37]M. S. Daw and M. I. Baskes, Phys. Rev. B **29**, 6443 (1984).
[38]S. Xu, E. Hwang, W.-R. Jian, Y. Su, and I. J. Beyerlein, Intermetallics **124**, 106844 (2020).
[39]S. Rao, B. Akdim, E. Antillon, C. Woodward, T. Parthasarathy, and O. N. Senkov, Acta Mater. **168**, 222 (2019).
[40]C. Varvenne, A. Luque, W. G. Nöhring, and W. A. Curtin, Phys. Rev. B **93**, 104201 (2016).
[41]W. G. Nöhring and W. A. Curtin, Modell. Simul. Mater. Sci. Eng. **24**, 045017 (2016).
[42]Y. N. Osetsky and D. J. Bacon, Modell. Simul. Mater. Sci. Eng. **11**, 427 (2003).
[43]S. Xu, Y. Su, and I. J. Beyerlein, Mech. Mater. **139**, 103200 (2019).
[44]S. Xu, J. R. Mianroodi, A. Hunter, B. Svendsen, and I. J. Beyerlein, Int. J. Plast. **129**, 102689 (2020).
[45]W.-R. Jian, S. Xu, and I. J. Beyerlein, Comput. Mater. Sci. **188**, 110150 (2021).
[46]B. A. Szajewski and W. A. Curtin, Modell. Simul. Mater. Sci. Eng. **23**, 025008 (2015).
[47]W.-R. Jian, M. Zhang, S. Xu, and I. J. Beyerlein, Modell. Simul. Mater. Sci. Eng. **28**, 045004 (2020).
[48]S. Xu (2026). "Local slip resistances in body-centered cubic random alloys," GitHub. https://github.com/shuozhixu/JVSTA_2026